Sensors & Actuators: B. Chemical 374 (2023) 132783

Contents lists available at ScienceDirect

Sensors and Actuators: B. Chemical

journal homepage: www.elsevier.com/locate/snb

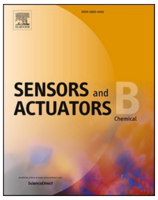

Enhanced ZIF-8-enabled colorimetric CO_2 sensing through dye-precursor synthesis

Adrian K. Davey [a,b], Zhou Li [a,b], Natalie Lefton [a], Branden E. Leonhardt [a], Alireza Pourghaderi [a,b], Stuart McElhany [a,b], Derek Popple [c,d,e], Chunhui Dai [c,d,e], Salman Kahn [c,d,e], Matthew N. Dods [a], Alex Zettl [c,d,e], Carlo Carraro [a,b], Roya Maboudian [a,b,*]

[a] *Department of Chemical and Biomolecular Engineering, University of California, Berkeley, CA 94720, United States*
[b] *Berkeley Sensor & Actuator Center, Berkeley, CA 94720, United States*
[c] *Department of Physics, University of California, Berkeley, CA 94720, United States*
[d] *Materials Sciences Division, Lawrence Berkeley National Laboratory, Berkeley, CA 94720, United States*
[e] *Kavli Energy NanoSciences Institute at the University of California Berkeley and the Lawrence Berkeley National Laboratory, Berkeley, CA 94720, United States*

ARTICLE INFO

Keywords:
Indoor air quality
Volatile organic compound
in-situ ultraviolet-visible (UV-Vis) spectroscopy
Dye-precursor synthesis

ABSTRACT

The accumulation of carbon dioxide (CO_2) within enclosed spaces, along with volatile organic compounds, under certain humidity, temperature, and ventilation conditions is associated with detrimental human health symptoms such as fatigue. Color-based chemical sensing is a promising approach to detect CO_2 levels relevant to indoor air quality through producing fast, quantifiable output visible to the naked eye. In a prior work, a colorimetric gas sensor was fabricated through synthesizing the metal-organic framework, ZIF-8, as the adsorbent, followed by post-synthetic mixing with a dye, phenol red (PSP), and primary amine, ethylenediamine (ED). While this sensor (termed PSP-ED/ZIF-8) maintained its structural integrity in atmospheric conditions and exhibited an increasing fuchsia-to-yellow color change with increasing CO_2 levels in dry environment, the colorimetric response greatly suffered in the presence of humid CO_2. In this work, a significantly improved colorimetric CO_2 sensor (referred to as ED/PSP:ZIF-8) is accomplished through *directly* incorporating phenol red in the ZIF-8 metal and linker precursor solutions and then blending with ethylenediamine. MATLAB-generated color distributions and *in-situ* ultraviolet-visible (UV-Vis) spectroscopic studies quantitatively demonstrate an enhanced colorimetric gas response of ED/PSP:ZIF-8 compared to that of PSP-ED/ZIF-8 across an important range of CO_2 for indoor air quality monitoring (500 – 3500 ppm) and across a range of humidity. The new sensor also exhibits high selectivity to CO_2 compared to select volatile organic compounds, such as acetone and ethanol, which contribute to human health symptoms experienced indoors. The enhanced performance is attributed to the proposed incorporation of phenol red within ZIF-8, while maintaining the chemical stability of the MOF.

1. Introduction

While global industrial operations continue to account for scores of pollutants emitted into the atmosphere, the associated consequences for human and environmental health remain a major concern in the 21st century [1,2]. These burgeoning emissions—consisting of various species such as particulate matter, nitrogen dioxide, and carbon dioxide (CO_2)—impose deleterious conditions on the human cardiovascular and respiratory systems, which can develop into acute diseases resulting in shortened life expectancy [1,2]. Of these airborne molecules, CO_2 has been a target gas of particular interest to scientists whose various studies in such areas as chemical sensing [3] and separation and capture [4] elucidate chemical and physical processes that inform relationships between CO_2 and the collective wellness of life on the planet [1].

Given that humans spend most their lives in enclosed spaces, such as homes [5] and commercial buildings [6], indoor air quality should be optimized for their overall wellbeing. As a natural product of human metabolism [5], CO_2 is a common species existent within indoor settings. However, the accumulation of certain levels of CO_2 indoors introduces specific harms to occupants [5,6]. While indoor CO_2 levels have been as low as ~400 parts per million (ppm) in certain environments, prior research has linked prolonged exposure to concentrations

---

* Corresponding author at: Department of Chemical and Biomolecular Engineering, University of California, Berkeley, CA 94720, United States.
E-mail address: maboudia@berkeley.edu (R. Maboudian).

https://doi.org/10.1016/j.snb.2022.132783
Received 18 July 2022; Received in revised form 20 September 2022; Accepted 1 October 2022

in the range of 1000 and 2500 ppm with reduced decision-making performance [7]. Since indoor CO_2 concentrations can feasibly reach 3000 ppm [8] (depending on the number of occupants and ventilation rate), the U.S. Occupational Health and Safety Administration (OSHA) recommends a maximum of 5000 ppm CO_2 as a time-weight average (TWA) for an 8 hr workday [7]. However, discrepancies exist in the literature on whether pure CO_2 (or its airborne coexistence with other bioeffluents, such as volatile organic compounds, VOCs) is responsible for compromised human cognitive function indoors [8–10]. Despite these contentions, previous studies attribute indoor CO_2, VOCs, temperature, humidity, and improper ventilation collectively to *sick building syndrome (SBS)*, which defines a group of symptoms including headaches and decreased productivity [11,12]. In recent decades, efforts to minimize energy consumption have led to decreased ventilation rates in some indoor spaces, resulting in the accumulation of CO_2 and associated pollutants linked to SBS [7,9]. Moreover, rising atmospheric CO_2 levels (reported to have approached near 420 ppm in 2021) from industrial activities vented indoors could further contribute to SBS symptoms for building occupants [13].

The ongoing coronavirus disease 2019 (COVID-19) pandemic has necessitated increased periods indoors to prevent the spread of the virus [14–16]. In certain cities with lockdown measures, residents experienced prolonged exposure to CO_2, VOCs, and other indoor pollutants, which is ascribed to the heightened use of cleaning agents and insufficient ventilation from civic strategies to conserve energy [7,9,14]. Of those who contracted and recovered from COVID-19, some have developed “Long-COVID,” which describes the persistence of symptoms post-initial infection, such as fatigue, loss of smell, shortness of breath, confusion, and chest pain [17,18]. As more COVID-19 variants emerge and scientists ascertain their long-term effects on human sensory capabilities, the design and operation of optimal indoor pollutant sensors is imperative for the improvement of human wellness in enclosed spaces [17,18].

This paper focuses on CO_2 as a purported indoor air pollutant. Toward detecting indoor CO_2 levels, the desired sensor should be low-cost, simple to operate, non-responsive to other indoor pollutants, and capable of exhibiting a signal clear to the naked eye [19]. The common indoor CO_2 monitor is based on the nondispersive infrared (NDIR) technique, which screens wavelength absorption in the infrared region of the electromagnetic spectrum resonant with the IR-active vibrational modes of target gases [20]. While NDIR technologies demonstrate longevity, these devices characteristically have been limited by their bulky dimensions and high cost [20,21]. Colorimetry, however, offers simple and scalable fabrication, low-cost operation, quick response times, and obvious signal to the human eye [22,23].

In a previous paper [24], we introduced a colorimetric CO_2 sensor composed of a porous adsorbent, a dye, and a primary amine (in methanol) drop-cast on cellulose filter paper. The adsorbent was based on a metal-organic framework (MOF), which constitutes a class of porous, crystalline materials composed of metal nodes coordinated by organic linkers with large surface areas and tunable pore chemistries suitable for applications in chemical sensing [24,25]. For this application, we selected a zeolitic imidazolate framework (ZIF), which is a class of MOFs consisting of metal cations tetrahedrally-coordinated to imidazolate linkers structured with “zeolite-like” topologies [24,26,27]. The specific ZIF, ZIF-8, is composed of zinc (Zn^{2+}) cations coordinated to 2-methylimidazolate (mIm^-) linkers with 3.4 Å six-member pore windows and 11.6 Å pore cages accessible to small molecules such as CO_2 [24,26,27]. In addition to its simple room temperature synthesis and chemical stability, ZIF-8 was selected because of its documented selectivity to CO_2 in binary gas mixtures [26,27], as well as prior simulations associating preferential CO_2 adsorption sites with positions near the imidazolate linker [24,28]. In addition to the ZIF-8 adsorbent, the colorimetric gas sensor consisted of (a) the dye, phenol red (PSP), whose color transitioned from fuchsia ($\lambda_{max} \sim 570$ nm) in basic environment to yellow ($\lambda_{max} \sim 443$ nm) in acidic environment [24,29,30], as well (b) the primary amine, ethylenediamine [ED], which has been used in other studies toward enhanced CO_2 absorption and adsorption [24,31].

The first-generation colorimetric CO_2 sensor, termed PSP-ED/ZIF-8, demonstrated several feats. Upon post-synthetically mixing ZIF-8 with PSP and ED, the structural integrity of ZIF-8 was maintained for four weeks [24]. Colorimetric assays demonstrated a sensitivity to dry CO_2 levels as low as 700 ppm, with increasing purple-to-yellow color intensity as CO_2 levels were increased to 7500 ppm [24]. Moreover, in the absence of ZIF-8, no color change was observed on cellulose filter paper [24]. The change in color intensity was quantified as a function of CO_2 concentration using an *ex-situ* ultraviolet-visible (UV-Vis) spectroscopic technique, which used the 443 and 570 nm reflectance (% R) peaks attributed to phenol red [24]. However, in the presence of humidity, both colorimetric assays and *ex-situ* UV-Vis spectroscopic analyses exhibited a largely diminished colorimetric CO_2 response [24].

In this paper, we present a second-generation sensor (referred to as ED/PSP:ZIF-8) based on *dye-precursor synthesis*, which involves directly mixing phenol red with the ZIF-8 metal and linker precursor solutions to form dye-loaded ZIF-8 (called PSP:ZIF-8), and then incorporating ethylenediamine to complete the sensor. Given the realistic concentrations of CO_2 that can develop in enclosed spaces with varied occupants and ventilation [8], the sensors are exposed to 540–3500 ppm CO_2 (in both dry and humid conditions). Furthermore, in contrast to the *ex-situ* UV-Vis spectroscopic technique shown in the prior work [24], here we employ an *in-situ* UV-Vis spectroscopic method toward a more accurate and efficient colorimetric gas sensing. *In-situ* UV-Vis spectroscopy and MATLAB-generated color parsing quantitatively reveal an improved colorimetric CO_2 response (across humidity) of the ED/PSP:ZIF-8 material compared to that of the PSP-ED/ZIF-8. To quantitatively assess the colorimetric CO_2 sensing fitness of ED/PSP:ZIF-8 in the presence of other indoor air pollutants, *in-situ* UV-Vis spectroscopy and optical measurements are also conducted using acetone and ethanol, which illustrate the negligible impact of VOCs on the sensor’s affinity for CO_2.

2. Experimental section

2.1. Sensing material synthesis

PSP-ED/ZIF-8 synthesis follows the process described previously [24]. 1.04 g of zinc nitrate hexahydrate [$Zn(NO_3)_2 0.6\ H_2O$; Fischer Scientific] and 1.04 g of 2-methylimidazole (Hmim, 99%, Sigma-Aldrich) are sonicated in 60 ml of methanol (Fischer Chemical) in separate beakers [24]. Then, the 2-methylimidazole methanolic solution is slowly poured into the zinc nitrate hexahydrate solution and allowed to react overnight in an unstirred environment [24]. The resulting ZIF-8 crystals are obtained *via* centrifugation (12,000 rpm for 5-min) and washed three times in methanol [24]. Once the ZIF-8 crystals are collected, 400 µl of ethylenediamine (Sigma-Aldrich) are poured into 19.6 ml of methanol, and 10 mg of phenolsulfonpthalein (Acros Organics) are dissolved into this solution [24]. Pristine ZIF-8 crystals are then dissolved into this mixture to form an 80 mg/ml solution of PSP-ED/ZIF-8 [24]. The fabrication process is shown in Fig. S1.

For the synthesis of ED/PSP:ZIF-8, 2.08 g of zinc nitrate hexahydrate ($Zn(NO_3)_2.6H_2O$; Fischer Scientific) and 2.08 g of 2-methylimidazole (Hmim, 99%, Sigma-Aldrich) are dissolved in 120 ml of methanol (Fischer Chemical) in separate beakers through prolonged sonication (Crest Ultrasonics). Then, 60 mg of phenol red are added to the zinc precursor solution and 60 mg of phenol red are added to the imidazolate precursor solution. After sonicating these solutions, the phenol red/imidazolate precursor solution is poured into the phenol red/zinc precursor solution and allowed to react at room temperature for 48 h (with no stirring). The resulting crystals, termed PSP:ZIF-8, are separated from the methanolic supernatant through slowly pouring into a disposable scintillation vial (Trident technology (Jiangsu)Co., Ltd.). Then, a 2% ethylenediamine (99%, Sigma-Aldrich) solution (% v/v) in methanol is produced by adding 100 µl of ethylenediamine to 4.9 ml of methanol.

This solution is then blended with the PSP:ZIF-8 crystals to form an 80 mg PSP:ZIF-8/ml solvent mixture. This fabrication process is displayed in Fig. S2.

2.2. Materials characterization methods

Powder X-ray diffraction (PXRD) patterns are accomplished using a Bruker diffractometer (Cu K-α radiation, $\lambda = 1.54$ Å, 40 kV, 40 mA) [24]. Morphological information about the synthesized materials is acquired using scanning electron microscopy, SEM (Zeiss Gemini Ultra55 Field Emission SEM) at an operating voltage of 5 kV. Samples are drop-cast on silicon chips, and sputter coated with Au (10.0 nm) for 7-min to provide appreciable electrical conductivity prior to collecting SEM imaging data. ZIF-8-based sensors are dispersed in isopropyl alcohol by bath sonication for 15 min and drop-cast onto copper/lacey carbon grids for transmission electron microscopy (TEM) imaging. TEM imaging is carried out on a JEOL-2010 microscope operated at 80 keV. Particle size distributions are completed using Fiji imaging software. Fourier transform infrared (FTIR) transmittance data are collected (spectral range: 4000–400 cm^{-1}; resolution: 4 cm^{-1}) using a Bruker Vertex80 FTIR instrument. Brunaeur-Emmett-Teller (BET) surface analysis and pore size distribution measurements (N_2 at 77 K) are accomplished using a Micromeritics Gemini VII Surface Area and Porosity instrument. Prior to BET measurements, 80 mg/ml solutions of ZIF-8-based samples are centrifuged, separated from the supernatant, and dried at room temperature (21.5 ± 0.3 ℃ at 49.8 ± 1% RH). The resulting powders are then degassed at 150 °C overnight using a Micromeritics VacPrep 061 Sample Degas System.

2.3. Gas sensing characterization

In-situ ultraviolet-visible diffuse reflectance spectroscopy with an Evolution 300 UV-Vis (Thermo Scientific) spectrophotometer (spectral range: 400–600 nm; bandwidth: 1.0 nm; scan speed: 60 nm/min) is used to quantify the color change upon controlled exposure to CO_2. Sample deposition onto cellulose filter paper (VWR North American) and insertion into the spectrophotometer closely follows the procedure reported in the prior work [24]. Specifically, a 0.7 cm × 0.7 cm piece of cellulose filter paper is attached to the UV-Vis sample enclosure *via* double-sided carbon black tape (Ted Pella, Inc.), inserted into the UV-Vis chamber, and used as a reflectance (% R) background [24]. Then, 20 ul of PSP-ED/ZIF-8 or ED/PSP:ZIF-8 is drop-cast on another piece of 0.7 cm × 0.7 cm cellulose filter paper, dried for 120 s, and placed into the UV-Vis spectrophotometer for *in-situ* target gas exposure [24].

The *in-situ* UV-Vis measurements under controlled CO_2 exposures proceed as illustrated in Fig. S3. A CO_2 cylinder (Airgas; 0.995 mol% CO_2 in N_2), dry air cylinder (Praxair; 79 mol% N_2; 21 mol% O_2), and acetone cylinder (Airgas; 0.1001 mol% $(CH_3)_2CO$ in N_2) are attached to a gas line. To achieve the desired CO_2 levels, the gas valves (shown in red) are opened and needle valves particular to the inlet CO_2 and dry air flows are adjusted to attain desired flowrates (plotted in Fig. S4). Once the gases are mixed, they are channeled through either (a) a continuous stream that maintains dry conditions (indicated in Fig. S3 with a downward yellow arrow) or (b) a bubbler to adjust the relative humidity (indicated in Fig. S3 with an upward blue arrow). The resulting mixture is fed into the UV-Vis chamber until steady-state is reached after about 7 min (Fig. S5). The total gas flow rate (set at 300 ml/min) composed of a given concentration of CO_2 and air flow rates is measured using an Agilent Technologies ADM2000 Universal Gas Flowmeter. As shown in Fig. S3, each CO_2 concentration (and corresponding humidity value) is calibrated with a wireless GasLab Plus CM-501 NDIR sensor (contained within a sealed plastic vessel). Dry and humid conditions are taken to be 0.133 ± 0.8% RH and 45.4 ± 3% RH, respectively, at 23.5 ± 1 ℃.

Once the sensor-coated filter paper is placed inside the UV-Vis spectrophotometer, the sensor is exposed to a specific CO_2 concentration and humidity using the methods described above [24]. After steady-state is reached, a reflectance (% R) *vs.* wavelength (nm) profile is collected [24]. Each diffuse reflectance value is then converted into a Kubelka-Munk value, F(R) (shown as Eq. 1), consisting of the absorption coefficient (K) and scattering coefficient (S) [24,32].

$$F(R) = \frac{(1-R)^2}{2R} = \frac{K}{S} \tag{1}$$

In the diffuse reflectance UV-Vis spectra, phenol red changes color from violet ($\lambda_{max} \sim 570$ nm) under basic conditions to yellow ($\lambda_{max} \sim 443$ nm) under acidic conditions [24,29,30]. For each CO_2 exposure, the ratios of the respective 443 and 570 nm F(R) values are depicted as scatter plots as a function of CO_2 concentration (ppm) [24].

Toward probing the long-term gas sensing performance and sensor stability in variable humidity, additional *in-situ* UV-Vis spectra are collected in which sensors (25 µl drop-cast on cellulose filter paper) are exposed to 3500 ± 300 ppm CO_2 (total gas flow rate: 300 ml/min). All trials are collected at room temperature (23.0 ± 0.8 ℃) and in dry (0% RH) and humid (82.0 ± 5% RH) environments. Colorimetric 443/570 nm F(R) ratios are tabulated for up to 120 min of exposure to CO_2. After that, the sensor is exposed to 300 ml/min dry air for 20 min. Subsequently, the dry air is turned off for an additional 20 min. At this time, another "0-min" spectrum is obtained, and the sensor is exposed to 3500 ppm CO_2 again at different times for 120 min. For this experiment, three cycles are collected (in dry and humid environment). Following multiple hours of repeated *in-situ* UV-Vis spectroscopic measurements, ZIF-8 stability on cellulose filter paper is analyzed using FTIR spectroscopy.

To evaluate the effect of VOCs on colorimetric CO_2 sensing, the same *in-situ* UV-Vis dosing experiments (described in Fig. S3) are performed using acetone (Airgas; 0.1001 mol% $(CH_3)_2CO$ in N_2). Given the emergence of nasal, throat, and optic irritation from acetone exposure, the U. S. National Institute for Occupational Safety and Health (NIOSH) recommended exposure limit/time weight average (REL/TWA) for this gas is 250 ppm [33]. In this study, the acetone concentration up to 314 ppm is probed. The acetone flow rate is varied while maintaining a set CO_2 concentration (in 450–3600 ppm range) and a total gas flow rate of 350 ml/min. Eq. 2 demonstrates how these selected acetone flow rates are converted to respective concentrations in ppm.

$$[Ac]_{UV-Vis} = \frac{[Ac]_{cylinder} * Ac_{flowrate}}{TG_{flowrate}} \tag{2}$$

where:

$[Ac]_{UV\text{-}Vis}$ = concentration of acetone in the *in-situ* UV-Vis chamber (ppm)
$[Ac]_{cylinder}$ = concentration of acetone in the cylinder (1000 ppm)
$Ac_{flowrate}$ = flow rate of acetone/nitrogen stream (ml/min)
$TG_{flowrate}$ = total gas flow rate entering the UV-Vis chamber (350 ml/min).

In addition to the *in-situ* UV-Vis spectroscopic technique, optical images of both sensors (in variable CO_2 and humid environments) are obtained and then read into a MATLAB script for subsequent analysis [24]. First, 20 µl of the sensing solutions are drop-cast on cellulose filter paper and allowed to dry in ambient air (453 ± 2 ppm CO_2; 40.6 ± 2% RH; 27.7 ± 0.7 °C) for 120 s [24]. The same LabView-controlled gas manifold system described in prior work is used for qualitative color change studies, consisting of house air, an evaporator system, pressure swing adsorption dryers, mass flow controllers (Bronkhorst), and target gases [24]. A cylinder of 50,380 ppm CO_2 balanced in nitrogen (Praxair) is used for colorimetric imaging [24]. Toward qualitatively assessing the role of select VOCs on the observed color change (in dry conditions), a 978 ppm ethanol cylinder (Praxair; balanced in nitrogen) and 400 ppm acetone (Praxair; balanced in nitrogen) cylinder are used. Similar to the human health symptoms borne from acetone exposure [33], ethanol is associated with nasal and optic irritation, resulting in a NIOSH REL/TWA of 1000 ppm [34]. For these colorimetric imaging assays, the total gas flow rate is kept constant at 300 standard cubic centimeters per minute (sccm) and the corresponding humidity values are measured at ambient temperature (27.7 ± 0.7 °C). Select CO_2 and humidity levels are validated using a wireless GasLab Plus CM-501 NDIR sensor [24].

For a given CO_2 concentration and humidity (or VOC exposure), each sensor is directly exposed for 20 s. Progressive color changes are recorded using a Google Pixel 4 XL smartphone [24]. From these videos, “Before controlled exposure” and “Exposed” images are prepared and downloaded into a MATLAB script as 1.7” x 1.7” squares [24]. Color output is produced as a 162 × 162-pixel red-green-blue (RGB) distribution [24]. RGB values are obtained with the Y-axis held constant at pixel 81, with the X-axis sweeping from pixels 60–100 [24].

3. Results and discussion

3.1. Material characterization

Fig. 1 shows the collected PXRD patterns from the simulated pristine ZIF-8 (refcode: VELVOY) [35], synthesized pristine ZIF-8, PSP-ED post synthetically added to ZIF-8 (PSP-ED/ZIF-8), PSP added to ZIF-8 precursor solution (PSP:ZIF-8), and ED added to PSP:ZIF-8 (ED/PSP:ZIF-8). In all samples, the diffraction peaks are consistent with the expected sodalite structure of ZIF-8 reported in the literature [24,36]. However, small peak shifts are observed with the PSP:ZIF-8 and ED/PSP:ZIF-8 materials compared to the pristine ZIF-8 and PSP-ED/ZIF-8 materials. Computational methods examining the structure and stability of ZIF-8 suggest that this observation could be ascribed to emergent defects within the lattice [37], such as from linker vacancies and dangling linkers, which could result in strain of the ZIF-8 lattice when synthesized with PSP. Moreover, the addition of ethylenediamine to form PSP-ED/ZIF-8 and ED/PSP:ZIF-8 produces a change in relative XRD peak intensities compared to those of pristine ZIF-8 and PSP:ZIF-8. As has been observed with metal-organic frameworks loaded with C_{60} fullerenes [38] and with adsorbed benzene [39], the changes in relative XRD peak intensities between the first- and second-generation sensors may be attributed to the changes in electron density along crystallographic planes upon ethylenediamine incorporation onto the MOF.

SEM images of pristine ZIF-8, PSP-ED/ZIF-8, PSP:ZIF-8, and ED/PSP:ZIF-8 are depicted in Fig. 2. For the pristine ZIF-8 and PSP-ED/ZIF-8, ~100 nm nanocrystals are obtained, which is in agreement with reported room temperature methanolic ZIF-8 synthesis with similar metal: linker: precursor molar ratios [24,40]. Upon incorporation of phenol red into the ZIF-8 precursor mixture, however, the PSP:ZIF-8 (and ED/PSP:ZIF-8) crystals formed are significantly larger in size (~400 nm). In addition to the role of the modified duration of MOF synthesis [41], the change in reaction solution composition (with phenol red now mixed with ZIF-8 precursors in methanol) may result in a ZIF-8 growth favoring larger crystals [42]. TEM images for PSP-ED/ZIF-8 and ED/PSP:ZIF-8 are shown in Fig. 3. Whereas the average particle size for PSP-ED/ZIF-8 is 0.11 ± 0.03 µm, the ED/PSP:ZIF-8 particles are 0.43 ± 0.07 µm.

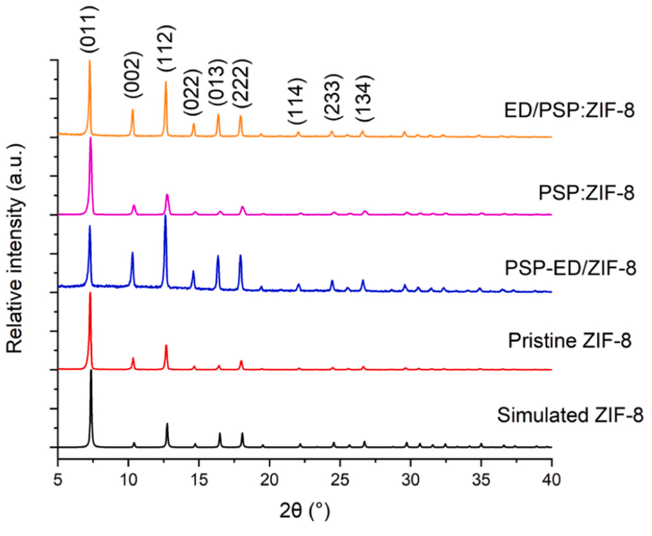

Fig. 1. Powder X-ray diffraction patterns (Cu *K*-α radiation, λ = 1.54 Å) of simulated ZIF-8 (VELVOY), pristine ZIF-8, PSP-ED/ZIF-8, PSP:ZIF-8, and ED/PSP:ZIF-8.

FTIR transmittance spectra for the gas sensing materials and their constituents are shown in Fig. S6**.** As listed in Table S1, the observed 421 cm^{-1} vibrational band in pristine ZIF-8, PSP-ED/ZIF-8, PSP:ZIF-8, and ED/PSP:ZIF-8 is associated with the Zn-N stretch of the ZIF-8. In addition, the bands at 2931 and 3135 cm^{-1-}observed in PSP-ED/ZIF-8 and ED/PSP:ZIF-8 samples are ascribed to the aliphatic and aromatic C-H stretches of the imidazolate ligand, respectively [42–44]. The broad band positioned at 3310 cm^{-1} is assigned to an -OH stretching mode from the methanol solvent [45]. Finally, the bands observed at 3280 and 3355 cm^{-1} are attributed to N-H stretching modes of ethylenediamine [45,46]. Consistent with the PXRD patterns, these FTIR spectra confirm the formation of ZIF-8, as well as its chemical stability in the presence of phenol red and ethylenediamine for both sensors, PSP-ED/ZIF-8 and ED/PSP:ZIF-8. Moreover, as evidenced *via* the preserved Zn-N 421 cm^{-1} mode shown in Fig. S7, both PSP-ED/ZIF-8 and ED/PSP:ZIF-8 remain stable in basic environment over multiple weeks. This chemical stability of ZIF-8 in basic environment is attributed to the linkage of soft imidazolate anions with soft Zn^{2+} cations, which hard-soft acid-base theory predicts an excellent metal-ligand bond strength toward good metal-organic framework stability [24,47].

3.2. Colorimetric analyses in dry environment

Colorimetric responses of PSP-ED/ZIF-8 and ED/PSP:ZIF-8 exposed to 300 sccm dry CO_2 are displayed in Fig. 4. With increasing CO_2 levels, both sensors exhibit an increased yellow intensity. However, compared to the modest responses of the first-generation PSP-ED/ZIF-8 material at 600 ppm CO_2 and above, those of the second-generation ED/PSP:ZIF-8 material indicate a stronger yellow color. Mean RGB intensities for these exposures are provided in Tables 1 and 2 for PSP/ED-ZIF-8 and ED/PSP:ZIF-8, respectively. For the first-generation PSP/ED-ZIF-8 sensor, the average G-values increase and the average B-values decrease with increasing dry CO_2 exposure, demonstrating a stronger fuchsia-to-yellow colorimetric transition. For the second-generation ED/PSP:ZIF-8 material, the mean R-values and mean G-values both increase with rising dry CO_2 exposures. In alignment with the colorimetric assays depicted in Fig. 4, the mean R- and G-values for the new ED/PSP:ZIF-8 material exposed to 600 ppm CO_2 and above, respectively, are significantly larger than those for the PSP-ED/ZIF-8 material, indicating a stronger color response.

Transient and repeated exposures to 2500 ppm CO_2 are displayed in Fig. S8**.** Similar to the results of Fig. 4, the ED/PSP:ZIF-8 exhibits a vibrant yellow color compared to that of PSP-ED/ZIF-8, indicating a stronger colorimetric gas response. Both sensors respond to CO_2 within 1 s, and achieve a full color change within 20–30 s. The quick response times, as well as sensitivity to < 1000 ppm dry CO_2 displayed in Fig. 4, are consistent with reported ambient colorimetric CO_2 detection using dye- and tertiary amino alcohol-loaded porous adsorbents [19]. However, whereas the latter sensors are reversible [19], PSP-ED/ZIF-8 and ED/PSP:ZIF-8 only partially recover upon CO_2 removal (as shown in Figs. S4-C and S4-D) and sustain a residual yellow tinge compared to their pre-exposed states.

In addition to the color-based assays, quantitative results from the *in-situ* UV-Vis spectra for various CO_2 exposures are presented in Fig. 5. As the CO_2 level increases from 540 to 3350 ppm, the 443 nm F(R) peak

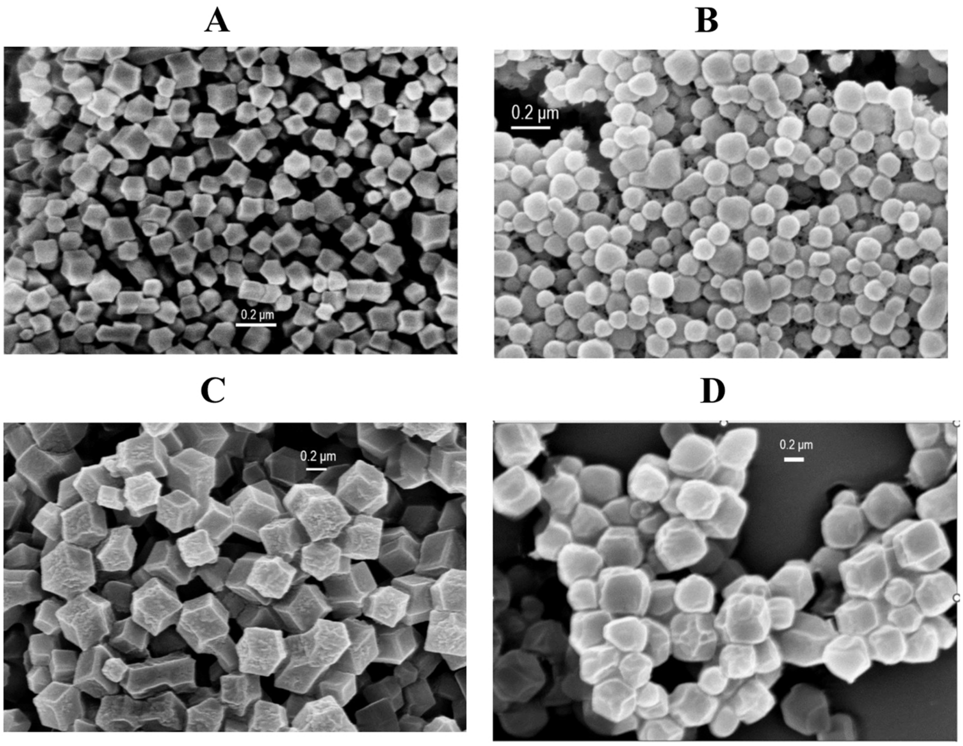

Fig. 2. SEM images for **(A)** Pristine ZIF-8, **(B)** PSP-ED/ZIF-8, **(C)** PSP:ZIF-8, and **(D)** ED/PSP:ZIF-8. Size bar: 0.2 μm.

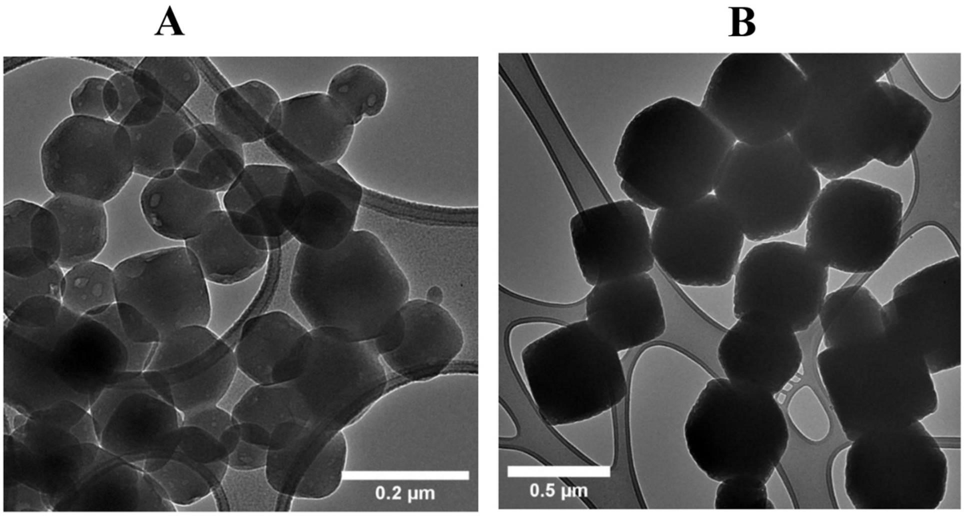

Fig. 3. TEM images for **(A)** PSP-ED/ZIF-8 (size bar: 0.2 μm) and **(B)** ED/PSP:ZIF-8 (size bar: 0.5 μm).

intensity rises relative to that at 570 nm for the PSP-ED/ZIF-8 material. However, for the new ED/PSP:ZIF-8 material, the 570 nm F(R) peak decreases relative to the 443 nm F(R) peak with increasing CO_2 levels. Colorimetric ratios of the 443 and 570 nm F(R) values *versus* CO_2 level (in ppm) are shown in Fig. 6. For both sensors, the ratios expectedly increase with rising CO_2 concentrations as the fuchsia-to-yellow color transition intensifies. However, as anticipated from the imaged exposures and RGB color distributions, the 443/570 nm F(R) ratios for the ED/PSP:ZIF-8 material are much larger than those of the PSP-ED/ZIF-8 material, similarly revealing a stronger colorimetric response to CO_2 in dry environment.

3.3. *Colorimetric analyses in humid environment*

Colorimetric profiles of PSP-ED/ZIF-8 and ED/PSP:ZIF-8 exposed to 1500 ppm CO_2 in 0%, 40%, and 80% relative humidity are depicted in Fig. 7. With increasing humidity, while the first-generation sensor scarcely provides a colorimetric CO_2 response at 40% RH and above, the second-generation sensor still exhibits a visible fuchsia-to-yellow transition compared to its “Before controlled exposure” at higher humidity. The effect of humidity on the colorimetric sensitivity to CO_2 is also portrayed in Tables 3 and 4. For the PSP-ED/ZIF-8 material, the R- and G-values both decrease with increasing humidity, with a significantly larger drop observed in the G-values. The ED/PSP:ZIF-8 material also exhibits reduced R- and G-values with increased humidity; however, these R- and G-values are markedly more intense than those of the PSP-

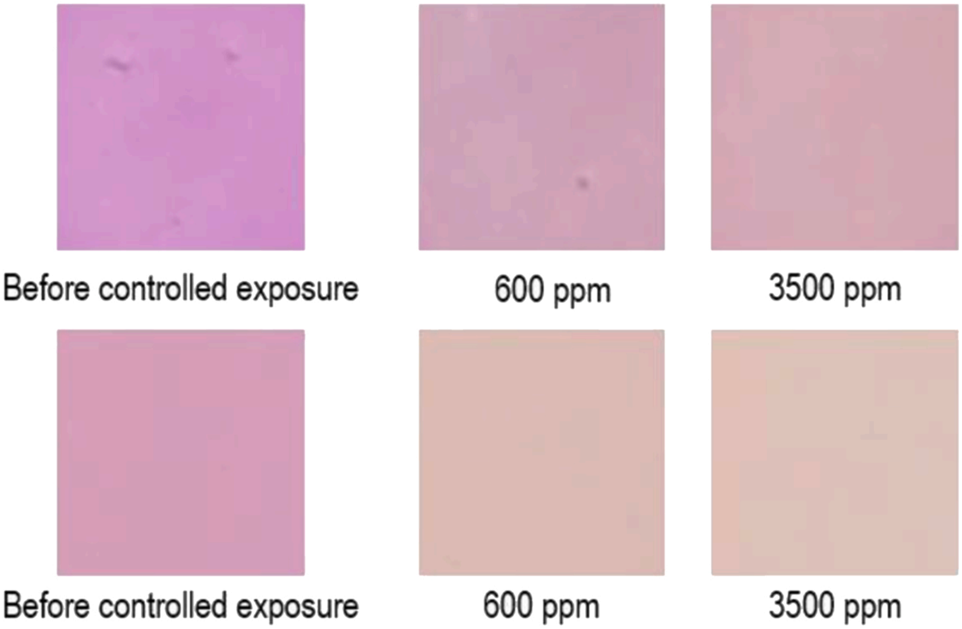

Fig. 4. Colorimetric images of sensors before controlled exposure under 0% relative humidity, exposed to 600 ppm CO_2, and 3500 ppm CO_2. **Top row**: PSP-ED/ZIF-8 (first-generation sensor). **Bottom row**: ED/PSP:ZIF-8 (second-generation sensor). Images are taken after 30 s of exposure.

Table 1
Mean RGB values for PSP-ED/ZIF-8 exposed to dry CO_2.

Exposure	Mean R-value	Mean G-value	Mean B-value
Before exposure	205 ± 0.7	145 ± 2.0	209 ± 1.0
600 ppm CO_2	203 ± 1.0	163 ± 1.0	187 ± 2.0
3500 ppm CO_2	209 ± 1.0	169 ± 1.0	183 ± 1.0

Table 2
Mean RGB values ED/PSP:ZIF-8 exposed to dry CO_2.

Exposure	Mean R-value	Mean G-value	Mean B-value
Before exposure	209 ± 0.7	158 ± 0.7	191 ± 1.0
600 ppm CO_2	215 ± 0.3	188 ± 0.8	182 ± 0.9
3500 ppm CO_2	218 ± 0.5	194 ± 0.3	187 ± 1.0

ED/ZIF-8 sensor at the same CO_2 concentration and humidity. Similarly, the B-values in dry and humid CO_2 conditions for the second-generation sensor are smaller than those for the first-generation sensor, indicating a stronger fuchsia-to-yellow color change.

Transient and repeated colorimetric imaging assays for PSP-ED/ZIF-8 and ED/PSP:ZIF-8 exposed to 2500 ppm CO_2 in 35% and 60% RH are shown in Figs. S9 and S10, respectively. Similar to their dry exposures, both sensors respond to humid CO_2 within seconds. However, with increased humidity, the colorimetric gas response is suppressed in both sensors (with that of ED/PSP:ZIF-8 outperforming that of PSP-ED/ZIF-8 at both moderate and elevated humidity). Finally, neither sensor completely recovers upon release from humid CO_2 environment, maintaining a slightly different color from its original state following four cycles of humid gas exposure.

Normalized F(R) profiles *versus* wavelength (in nm) are plotted in Fig. 8 as a function of CO_2 concentration under RH of 45.4 ± 3%. As the CO_2 exposures rise from 540 to 3350 ppm, the 443 nm F(R) peak intensity increases relative to that of the 570 nm F(R) peak for both first- and second-generation materials. Fig. 9 depicts these ratios as a function of humid CO_2 level. At any humid CO_2 concentration in this span, the colorimetric response is enhanced for the second-generation ED/PSP:ZIF-8 material relative to the first-generation PSP/ED-ZIF-8 material, with a sharp increase in the yellow intensity at higher CO_2 exposures. However, compared to colorimetric ratios achieved from the dry gas exposures displayed in Fig. 6, the 443/570 nm F(R) ratios in humid environment are smaller for both first- and second-generation sensors, establishing water as a sustained interferant in the colorimetric gas sensing mechanism [24].

Cyclic *in-situ* UV-Vis measurements of PSP-ED/ZIF-8 and ED/PSP:ZIF-8 exposed to 3500 ppm CO_2 (in 0% and 80% RH, respectively) are tabulated in Tables S2, S3, S4, and S5**.** As observed qualitatively from the colorimetric imaging assays, neither sensor fully recovers the 443/570 nm F(R) ratio ascribed to its pre-exposed state. The irreversible nature of both sensors upon gas exposure (across humidity) is largely attributed to the gradual evaporation of methanol upon deposition onto cellulose filter paper, which prevents either sensor from fully recovering its original color [24]. As shown in Table S2, PSP-ED/ZIF-8 maintains achieves similar quantitative color change responses to dry CO_2 in the first and second cycle. However, the colorimetric response comparatively decreases upon the third cycle. While PSP-ED/ZIF-8 exhibits a stronger quantitative color change to dry CO_2 (as evidenced in Table S3), the colorimetric response noticeably decreases with increased cycles. Upon prolonged exposure to humid CO_2 (in Table S4), PSP-ED/ZIF-8 exhibits an increase in its 443/570 nm F(R) ratio from the first to the second cycle, with a small increase from the second cycle to the third cycle. Finally, as depicted in Table S5, the ED/PSP:ZIF-8 similarly shows an increase in 443/570 nm F(R) ratios with increased cycling in humidity.

Following cyclic exposure to both dry and humid gas conditions, both sensors are scanned *via* FTIR spectroscopy to probe the stability of ZIF-8. Recent studies in the literature have illustrated how the structural integrity of ZIF-8 is compromised when submerged in pure water under specific mass ratios and ambient conditions for 24 h [48]. ZIF-8 hydrolysis has similarly been reported in water at higher temperatures [49]. In addition to structural degradation from prolonged immersion in water, ZIF-8 has also been shown to be vulnerable to structural degradation under prolonged exposure to acidic gases (such as CO_2) at elevated humidity [50]. Fig. S11 shows FTIR spectra of recovered PSP-ED/ZIF-8 and ED/PSP:ZIF-8 samples following cyclic exposure to dry and humid CO_2. The preserved 421 cm^{-1} Zn-N stretch in both the first- and second-generation sensors subsequent gas exposure indicates the stability of ZIF-8 to prolonged dry and humid CO_2 exposure.

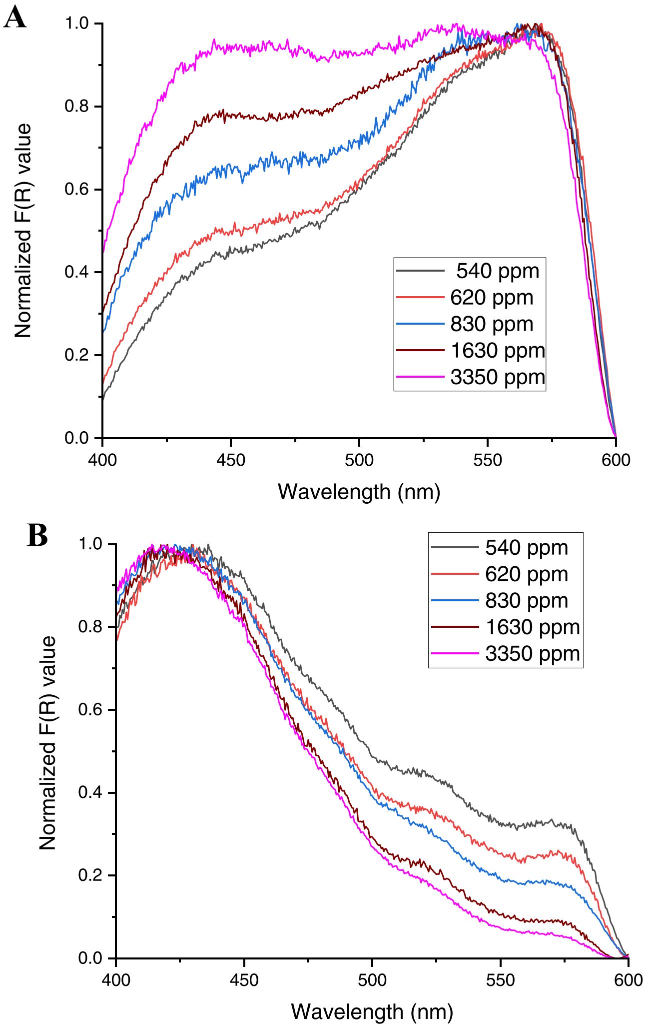

Fig. 5. Normalized F(R) values *versus* wavelength (nm) for dry CO_2 exposures. 540 ppm (black); 620 ppm CO_2 (red); 830 ppm (blue); 1630 ppm (wine); and 3350 ppm (magenta). **(A)** PSP-ED/ZIF-8 (first-generation sensor). **(B)** ED/PSP:ZIF-8 (second-generation sensor).

Compared to prior studies on ZIF-8 degradation, it is possible that the dilute CO_2 atmospheres exposed (resembling indoor air conditions), as well as the length of time exposed and mass of sensor deposited on the cellulose filter paper, do not readily induce a measurable collapse of the crystalline MOF network.

3.4. Sensors' responses to volatile organic compounds (VOCs)

To assess the role of other airborne pollutants (such as VOCs) as possible interferants in the colorimetric CO_2 sensing mechanism, colorimetric assays and *in-situ* UV-Vis spectra are collected in response to acetone and ethanol. Fig. S12 shows colorimetric images of the PSP-ED/ZIF-8 and ED/PSP:ZIF-8 materials exposed to dry house air (458 ± 3 ppm CO_2), as well as dry house air mixed with 200 ppm ethanol and 200 ppm acetone. Compared to humid CO_2 exposures, the presence of these select VOCs demonstrates a relatively negligible effect on the observed color change achieved in dry atmosphere. In addition to the colorimetric imaging results, Fig. S13 demonstrates the results of *in-situ* UV-Vis experiments with CO_2 (450–3600 ppm) mixed with dry air and acetone (0, 20, and 314 ppm) at a total gas flow rate of 350 ml/min. Unlike the spectra observed in a humid atmosphere, both sensors exhibit a high selectivity to CO_2 with rising acetone levels, with the ED/PSP:ZIF-8 material displaying a significantly stronger color change than the PSP-ED/ZIF-8 material.

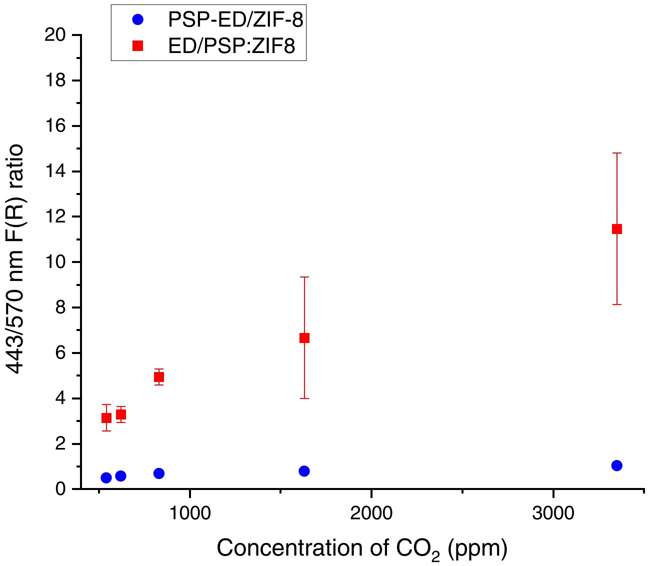

Fig. 6. 443/570 nm F(R) ratios for PSP-ED/ZIF-8 (blue) and ED/PSP:ZIF-8 (red) as a function of dry CO_2 exposure (in ppm). Standard deviation values are plotted as error bars which are smaller than the symbol size for PSP-ED/ZIF-8 sensor. For the ED/PSP:ZIF-8 material, the larger error bars observed at higher CO_2 concentrations are attributed to the high reflectance values achieved with increasing CO_2 levels (87% and up) as the sensor becomes more yellow.

3.5. Discussions of the sensing mechanism and differences between the two sensors

To understand the colorimetric CO_2 sensing behavior observed in dry and humid conditions, as well as in the presence of select VOCs, the zwitterion mechanism is described in this section. In the previous work [24], the zwitterion mechanism (characteristically used to evaluate the reaction chemistries involving CO_2 absorbed into aqueous primary and secondary amine solutions) was proposed to comprehend the color change dynamics involving ZIF-8, phenol red, and ethylenediamine in response to CO_2 and humidity in methanolic solvent [31,51,52]. Once adsorbed by ZIF-8, CO_2 is posited to first react with ethylenediamine (shown in Eq. 3 as RNH_2) to produce a zwitterion species [24,31,51,52].

$$CO_2 + RNH_2 \leftrightarrow RN^+H_2CO_2^- \tag{3}$$

Upon formation of the zwitterion, the second step of the reaction (shown as Eq. 4) ensues in which a base in the system, B, deprotonates the zwitterion to form a protonated species and carbamate species [24,31,51,52].

$$RN^+H_2CO_2^- + B \leftrightarrow RNHCO_2^- + BH^+ \tag{4}$$

At low humidity, the pH indicator, phenol red, is expected to function as the primary base and abstract the proton from the zwitterion species, thus modifying its conjugation and triggering a clear fuchsia-to-yellow color transition dependent on CO_2 concentration [24,29,30]. However, in humid conditions, water can participate in Eq. 4 as a free base to deprotonate the zwitterion [24,53]. Thus, it is hypothesized that adsorbed phenol red molecules might compete with water for access to the proton of the zwitterion, resulting in colorimetric suppression with increased humidity [24,53]. In addition, the intrinsic hydrophilicity of ethylenediamine [54] could promote water adsorption to the detriment of CO_2 adsorption, inhibiting formation of the zwitterion and thus disrupting the colorimetric gas response accomplished in dry environment [24].

Related to the cyclic *in-situ* UV-Vis results shown in Tables S2 and S3,

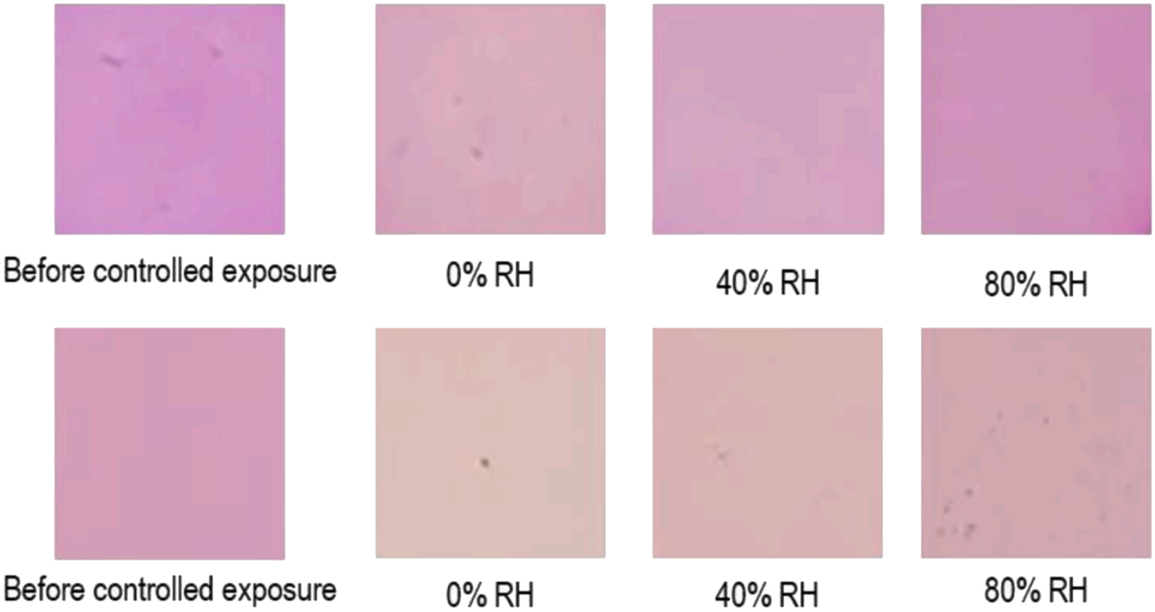

Fig. 7. Colorimetric images of sensors before controlled exposure, exposed to 600 ppm CO_2, under varied relative humidity. Top row: PSP-ED/ZIF-8 (first-generation sensor). Bottom row: ED/PSP:ZIF-8 (second-generation sensor). Images are taken after 30 s of exposure.

Table 3
Mean RGB values for PSP-ED/ZIF-8 exposed to 1500 ppm CO_2 in variable humidity.

Relative humidity (%)	Mean R-value	Mean G-value	Mean B-value
0	213 ± 2	171 ± 1	192 ± 1
40	208 ± 1	164 ± 1	196 ± 1
80	203 ± 1	148 ± 1	191 ± 1

Table 4
Mean RGB values for ED/PSP:ZIF-8 exposed to 1500 ppm CO_2 in variable humidity.

Relative humidity (%)	Mean R-value	Mean G-value	Mean B-value
0	216.0 ± 0.5	192.0 ± 0.7	186.0 ± 0.3
40	212.0 ± 0.4	180.0 ± 0.5	181.0 ± 0.5
80	205.0 ± 0.3	168.0 ± 0.5	178.0 ± 0.5

it is possible that the reduced colorimetric gas response observed with increased cycling can be ascribed to both the transient loss of methanol and formation of stable carbamates, which both age the sensor and limit the regeneration of ethylenediamine for subsequent CO_2 chemisorption [24,51–54]. However, as observed in Tables S4 and S5, it is possible that the dry air purge streams between cycles disrupt hydrogen bonding interactions between ethylenediamine and water in a humid gas environment, freeing more ethylenediamine molecules for subsequent CO_2 chemisorption and generating higher 443/570 nm F(R) ratios [54]. In contrast with these colorimetric studies using dye- and amine-modified ZIF-8 species, other amine-based systems exhibit an increased sensitivity to indoor levels of CO_2 in humid environment [55]. For example, a polymer blend of poly(ethylene oxide) and poly(ethyleneimine) coated onto a resonant mass sensor was proposed to demonstrate an enhanced indoor CO_2 detection in humid environment due to the availability of water molecules to convert carbamate species into stable bicarbonates, which provides free amines to bind additional CO_2 [55]. Given these differences, it is imperative to establish the specific interaction between ethylenediamine and water in these ZIF-8-based sensors, as well as possible competition between water and phenol red in the zwitterion deprotonation step during humid gas delivery [24,51–54]. However, with respect to mixed CO_2/VOC studies reported in Figs. S12 and S13, it is possible that neither acetone nor ethanol disturbs the chemisorptive interaction between CO_2 and ethylenediamine, nor functions as a competitive base for adsorbed phenol red species [24,51–53].

To understand the enhanced response to CO_2 observed in the second generation (ED/PSP:ZIF-8) sensor, the nature of phenol red and ethylenediamine adsorption onto ZIF-8 need to be evaluated between both sensors. While both sensors incorporate ethylenediamine through post-synthetic mixing with the MOF, the ED/PSP:ZIF-8 material involves the direct inclusion of phenol red into the ZIF-8 precursor broth, which results in the formation of nanocrystals more than triple the size of the pristine ZIF-8. In addition to understanding the role of synthetic phenol red mixing on ZIF-8 growth [42], the location of phenol red with respect to ZIF-8 between both sensors must be established. The structural flexibility of ZIF-8—associated with the "gate-opening" phenomenon describing a rotational swing of the imidazolate linkers to expand the 6-member ring pore aperture beyond its nominal 3.4 Å size—has been observed with penetrating liquids at high-pressure [56], as well as both computational and experimental studies involving the adsorption of gases with kinetic diameters exceeding 3.4 Å [57,58]. However, the ambient-pressure, room-temperature mixing of phenol red molecules with pristine ZIF-8 nanoparticles in methanol that produces the first-generation sensor is not anticipated to result in phenol red penetration through the ZIF-8 nominal pore aperture *via* the gate-opening phenomenon. Rather, it is expected that phenol red remains adsorbed on the external surface of the ZIF-8 adsorbent. However, in the case of the second-generation sensor, it is hypothesized that phenol red molecules, mixed with the ZIF-8 ligand and metal precursor solution in methanol, might become incorporated within the 11.6 Å pore cavities as ZIF-8 grows [26,27]. Prior studies on ZIF-8 have attributed preferential gas adsorption sites with regions proximate to the imidazolate linkers [28,59]. Given how ZIF-8 crystals grow in a phenol red-incorporated methanolic MOF precursor solution in the second-generation sensing approach, it is possible that dye molecules are well-distributed throughout the MOF and more proximate to CO_2-affinative regions of the linker than the first-generation sensor, triggering stronger colorimetric gas responses across humidity [28,59]. To test this hypothesis on comparative phenol red location on ZIF-8 between both sensors, the following set of experiments are conducted.

Fig. S14 shows the PSP-ED/ZIF-8 and ED/PSP:ZIF-8 materials after

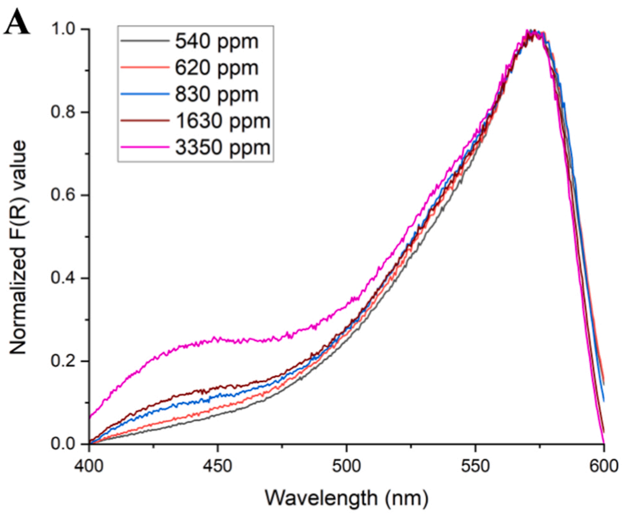

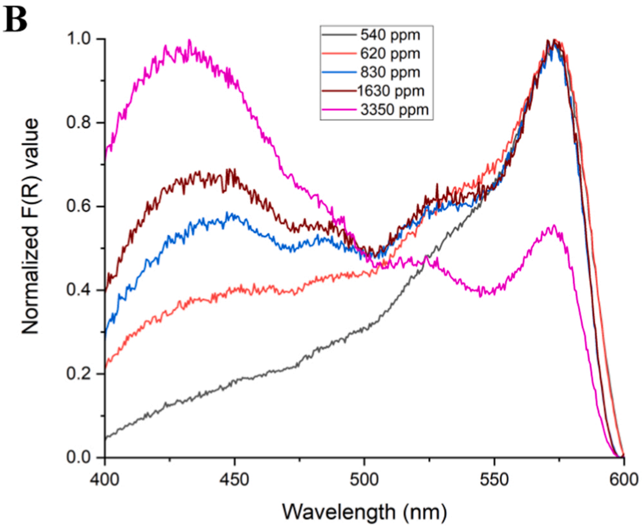

Fig. 8. Normalized F(R) values *versus* wavelength (nm) for humid CO_2 exposures (RH: 45.4 ± 3%). 540 ppm (black); 620 ppm CO_2 (red); 830 ppm (blue); 1630 ppm (wine); and 3350 ppm (magenta). **(A)** PSP-ED/ZIF-8 (first-generation sensor). **(B)** ED/PSP:ZIF-8 (second-generation sensor).

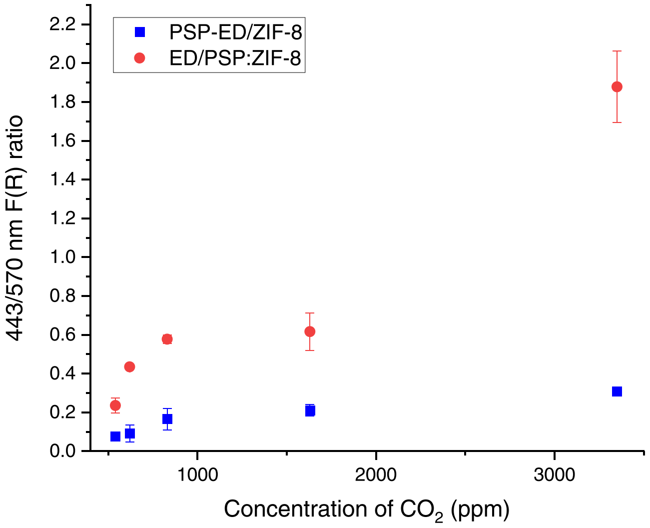

Fig. 9. 443/570 nm F(R) ratios for PSP-ED/ZIF-8 (blue) and ED/PSP:ZIF-8 (red) as function of CO_2 concentration (in ppm) under relative humidity of 45.4 ± 3%. Standard deviation values are plotted as error bars.

successive washes in methanol. Whereas the PSP-ED/ZIF-8 sensor becomes much lighter with increased washes, the ED/PSP:ZIF-8 sensor does not. The structural integrity of ZIF-8 is maintained upon washing, as displayed from the sustained 421 cm^{-1} Zn-N stretches shown in Fig. S15-A**.** With increased washes, the 1028 cm^{-1} C-O stretch associated with methanol emerges for both sensors [43]. Though the ZIF-8 structure is maintained, ethylenediamine is lost with successive washes. Figs. S15-B and S15-C show the disappearance of the 3280 and 3355 N-H stretches associated with ethylenediamine upon washing, which suggests that ethylenediamine is adsorbed to the external surface of the ZIF-8 adsorbent.

Toward estimating phenol red adsorption onto ZIF-8 between both materials, three samples (each) of PSP-ED/ZIF-8 and ED/PSP:ZIF-8 are (i) centrifuged, (ii) separated from their supernatant, (iii) rinsed with methanol for 60-min (in a sonication bath), (iv) centrifuged again, (v) separated again from their supernatant, and (vi) blended with methanol, a 2% ethylenediamine (by volume) methanolic solution, or a 0.5 mg/ml solution of phenol red dissolved in a 2% ethylenediamine (by volume) methanolic solution. Fig. S16 shows the response of these washed sensors to 800 ppm CO_2 (in dry conditions). When re-mixed with only methanol, neither sensor responds to CO_2. However, when re-mixed with ethylenediamine in methanol, the washed second-generation ED/PSP:ZIF-8 material demonstrates a strong fuchsia-to-yellow color change. On the other hand, the first-generation PSP-ED/ZIF-8 material turns white-yellow and shows minimal response to CO_2. When re-mixed with phenol red and ethylenediamine in methanol, though, the original PSP/ED-ZIF-8 material demonstrates a CO_2 response similar to that of its unwashed, fresh state. In other words, whereas the rinsed ED/PSP:ZIF-8 material only requires ethylenediamine (in methanol) to recover its colorimetric sensitivity to CO_2, the rinsed PSP-ED/ZIF-8 material requires *both* phenol red and ethylenediamine (in methanol). *These results support that ethylenediamine is bound to the external MOF surface for both sensors, whereas phenol red is incorporated within the internal surfaces of ZIF-8 in the second-generation sensor but on the external surface of ZIF-8 for the first-generation sensor*.

To further test the location of phenol red within ZIF-8 between the two sensors, an 80 mg/ml ZIF-8 solution is prepared by blending ZIF-8 with a 0.5 mg/ml phenol red solution (in methanol). Similar to the processes described above, this material—termed PSP/ZIF-8—is washed several times in methanol (for 30-min). The same process is performed using an 80 mg/ml PSP:ZIF-8 solution (in methanol). Fig. S17 shows how the PSP/ZIF-8 material becomes lighter with successive washes, transitioning from orange to light pink. In contrast, as shown in Fig. S18, the PSP:ZIF-8 material does not exhibit such a large color change with continued washing. Upon washing several times, the PSP/ZIF-8 and PSP:ZIF-8 materials are placed into the UV-Vis spectrophotometer and the reflectance (%R) at 570 nm is evaluated. As displayed in Table S6, the rinsed PSP/ZIF-8 material exhibits large increases in 570 nm reflectance values upon successive washes, suggesting loss of phenol red. However, the PSP:ZIF-8 material does not demonstrate such pronounced changes in its 570 nm reflectance value with continued washing, implying the retention of phenol red molecules and their incorporation within the internal surfaces of MOF.

Comparative surface area and micropore volume are shown for pristine ZIF-8 and PSP:ZIF-8 in Table 5**.** The reported BET surface area and micropore volume of pristine ZIF-8 are consistent with those in the literature [26,60,61]. BET surface area plots for the respective materials are displayed in Fig. S19**.** Relative to pristine ZIF-8, the formation of PSP:ZIF-8 results in crystals with a reduced BET surface area, Langmuir surface area, and micropore surface area, which could be ascribed to the incorporation of phenol red molecules into the micropores of ZIF-8. As shown in Fig. S20, the two micropores near 10 Å and 12 Å of PSP-ED/ZIF-8 and ED/PSP:ZIF-8 are consistent with reported ZIF-8 micropore widths [62,63]. However, as shown in Table 6**,** ED/PSP:ZIF-8 exhibits a decreased BET surface area compared to that of PSP-ED/ZIF-8, which could similarly be ascribed to phenol red

Table 5
BET surface area, Langmuir surface area, Dubinin-Astakhov micropore surface area, and Horvath-Kawazoe maximum pore volume for Pristine ZIF-8 and PSP:ZIF-8.

Material	BET surface area (m^2/g)	Langmuir surface area (m^2/g)	Dubinin-Astakhov micropore surface area (m^2/g)	Horvath-Kawazoe maximum pore volume at $p/p^\circ = 0.981$ (cm^3/g)
Pristine ZIF-8	1778.6	1933.0	1710.5	0.72
PSP:ZIF-8	1700.7	1794.6	1693.1	0.64

Table 6
BET surface area for PSP-ED/ZIF-8 and ED/PSP:ZIF-8.

Material	BET surface area (m^2/g)
PSP-ED/ZIF-8	1698.9
ED/PSP:ZIF-8	1631.6

Table 7
T-plot external surface area of Pristine ZIF-8, PSP-ED/ZIF-8, PSP:ZIF-8, and ED/PSP:ZIF-8.

Material	t-plot external surface area (m^2/g)
Pristine ZIF-8	177.4
PSP-ED/ZIF-8	58.5
PSP:ZIF-8	66.4
ED/PSP:ZIF-8	43.4

adsorption within the pore cage of ZIF-8. Finally, as shown in Table 7, the significant reduction of external surface area between the pristine ZIF-8 and PSP-ED/ZIF-8 could be assigned to the binding of phenol red to the external surface of ZIF-8 in this synthetic approach (rather than within the internal pores).

To expand on these experiments, the nature of interactions that inform phenol red and ethylenediamine adsorption onto ZIF-8 [64–67] will need to be studied in the future. Several spectroscopies, including second harmonic scattering techniques [68–71], nuclear magnetic resonance, X-ray-based, and vibrational techniques, will be pursued to elucidate the complex reaction mechanism involving ZIF-8, phenol red, ethylenediamine, CO_2, and humidity in methanol [72–74]. Through these experiments, the reaction products of the colorimetric gas sensing can be established, as well as the role of water as an interferant.

4. Conclusions

In this work, we successfully synthesized a second-generation, ZIF-8-based colorimetric CO_2 sensor from the direct mixing of the pH indicator, phenol red, with ZIF-8 precursors in a room temperature methanolic solvent. While PXRD patterns and FTIR spectra confirmed the chemical stability of this new sensor, ED/PSP:ZIF-8, MATLAB-generated RGB distributions and *in-situ* UV-Vis spectroscopy demonstrated an improved colorimetric CO_2 response in variable humidity and in presence of acetone and ethanol interferents, compared to that of the first-generation sensor, PSP-ED/ZIF-8. Additional experiments suggested that in the ED/PSP:ZIF-8 sensor, phenol red molecules were most likely incorporated in the interior of ZIF-8, while they resided on its external surface in the first-generation sensor, PSP-ED/ZIF-8. Future work will employ both vibrational and X-ray spectroscopies to understand colorimetric sensing differences between both PSP-ED/ZIF-8 and ED/PSP:ZIF-8, with emphasis on identifying differences in phenol red adsorption onto ZIF-8 and the role of water as an inhibitor for colorimetric gas sensing.

CRediT authorship contribution statement

Adrian K. Davey: Conceptualization, Data curation, Formal analysis, Funding acquisition, Investigation, Software, Validation, Writing – original draft. **Zhou Li:** Investigation, Writing – review & editing. **Natalie Lefton**: Investigation, Resources. **Branden E. Leonhardt:** Investigation, Resources. **Alireza Pourghaderi:** Investigation. **Stuart McElhany:** Investigation. **Derek Popple:** Resources, Software. **Chunhui Dai**: Investigation. **Salman Kahn:** Resources. **Matthew N. Dods:** Investigation, Resources, Writing – review & editing. **Alex Zettl:** Resources. **Carlo Carraro:** Writing – review & editing. **Roya Maboudian:** Conceptualization, Funding acquisition, Project administration, Resources, Supervision, Writing – review & editing.

Declaration of Competing Interest

The authors declare that they have no known competing financial interests or personal relationships that could have appeared to influence the work reported in this paper.

Data Availability

Data will be made available on request.

Acknowledgements

The authors gratefully acknowledge the support of the National Science Foundation in the form of a Graduate Research Fellowship (A.K. D.) and grant # 1903188, as well as the Bakar Fellows Program. The contributions of M.N.D. were supported by the U.S. Department of Energy, Office of Science, Office of Basic Energy Sciences under award DE-SC0019992. The authors also acknowledge the Lawrence Berkeley National Laboratory Catalysis Facility and Dr. Chithra Asokan for assistance with FTIR measurements. The gas sensing measurements were supported by the Director, Office of Science, Office of Basic Energy Sciences, Materials Sciences and Engineering Division, of the US Department of Energy under contract no. DE-AC02–05-CH11231, within the Nanomachines Program (KC1203). Transmission electron microscopy was also supported by the U.S. Department of Energy, Office of Science, Office of Basic Energy Sciences, Materials Sciences and Engineering Division, under Contract No. DE-AC02–05-CH11231 within the van der Waals Heterostructures Program (KCWF16). Work at the Molecular Foundry was supported by the Office of Science, Office of Basic Energy Sciences, of the U.S. Department of Energy under Contract No. DE-AC02–05CH11231.

Appendix A. Supporting information

Supplementary data associated with this article can be found in the online version at doi:10.1016/j.snb.2022.132783.

References

[1] H.M.A. Siddique, A.K. Kiani, Industrial pollution and human health: evidence from middle-income countries, Environ. Sci. Pollut. Res 27 (2020) 12439–12448, https://doi.org/10.1007/s11356-020-07657-z.

[2] R.M. Doherty, M.R. Heal, F.M. O'Connor, Climate change impacts on human health over Europe through its effect on air quality, Environ. Health 16 (Suppl 1) (2017) 118, https://doi.org/10.1186/s12940-017-0325-2.

[3] K.S.V. Santhanam, N.N.N. Ahamed, Greenhouse gas sensors fabricated with new materials for climatic usage: a review, ChemEngineering 2 (2018) 38, https://doi.org/10.3390/chemengineering2030038.

[4] H. Yang, Z. Xu, M. Fan, R. Gupta, R.B. Slimane, A.E. Bland, I. Wright, Progress in carbon dioxide separation and capture: a review, J. Environ. Sci. 20 (1) (2008) 14–27, https://doi.org/10.1016/S1001-0742(08)60002-9.

[5] G.R. Ana, A.S. Alli, D.C. Uhiara, D.G. Shendell, Indoor air quality and reported health symptoms among hair dressers in salons in Ibadan, Nigeria, J. Chem. Health Saf. 26 (1) (2019) 23–30, https://doi.org/10.1016/j.jchas.2018.09.004.

[6] P. Batog, M. Badura, Dynamic of changes in carbon dioxide concentration in bedrooms, Procedia Eng. 57 (2013) 175–182, https://doi.org/10.1016/j.proeng.2013.04.025.

[7] U. Satish, M.J. Mendell, K. Shekhar, T. Hotchi, D. Sullivan, S. Streufert, W.J. Fisk, Is CO_2 an indoor pollutant? direct effect of low-to-moderate concentrations on human decision-making performance, Environ. Health Perspect. 120 (12) (2012) 1671–1677, https://doi.org/10.1289/ehp.1104789.

[8] S. Snow, A.S. Boyson, K.H.W. Paas, H. Gough, M.-F. King, J. Barlow, C.J. Noakes, M.C. schraefel, Exploring the physiological, neurophysiological, and cognitive performance effects of elevated carbon dioxide concentrations indoors, Build. Environ. 156 (2019) 243–252, https://doi.org/10.1016/j.buildenv.2019.04.010.

[9] K. Azuma, N. Kagi, U. Yanagi, H. Osawa, Effects of low-level inhalation exposure to carbon dioxide in indoor environments: a short review on human health and psychomotor performance, Environ. Int. 121 (2018) 51–56, https://doi.org/10.1016/j.envint.2018.08.059.

[10] X. Zhang, P. Wargocki, Z. Lian, C. Thyregod, Effects of exposure to carbon dioxide and bioeffluents on perceived air quality, self-assessed acute health symptoms, and cognitive performance, Indoor Air 27 (1) (2016) 47–64, https://doi.org/10.1111/ina.12284.

[11] A. Ghaffarianhoseini, H. AlWaer, H. Omrany, A. Ghaffarianhoseini, C. Alaluoch, D. Clements-Croome, J. Tookey, Sick building syndrome: are we doing enough, Archit. Sci. Rev. 61 (3) (2018) 99–121, https://doi.org/10.1080/00038628.2018.1461060.

[12] C.-J. Chang, H.-H. Yang, Y.-F. Wang, M.-S. Li, Prevalence of sick building syndrome-related symptoms among hospital workers in confined and open working spaces, Aerosol Air Qual. Res. 15 (2015) 2378–2384, https://doi.org/10.4209/aaqr.2015.01.0040.

[13] Web reference one. Carbon dioxide peaks near 420 parts per million at Mauna Loa observatory. U.S. Department of Commerce - National Oceanic and Atmospheric Administration. ⟨https://research.noaa.gov/article/ArtMID/587/ArticleID/2764/Coronavirus-response-barely-slows-rising-carbon-dioxide⟩ (accessed 2022/1/1).

[14] S. Domínguez-Amarillo, J. Fernandez-Agilera, S. Cesteros-Garcia, R.A. Gonzalez-Lezcano, Bad air can also kill: residential indoor air quality and pollutant exposure risk during the COVID-19 crisis, Int. J. Environ. Res. Public Health 17 (2020) 7183, https://doi.org/10.3390/ijerph17197183.

[15] C. Sun, Z. Zhai, The efficacy of social distance and ventilation effectiveness in preventing COVID-19 transmission, Sustain. Cities Soc. 62 (2020), 102390, https://doi.org/10.1016/j.scs.2020.102390.

[16] I.E. Isphording, N. Pestel, Pandemic meets pollution: Poor air quality increases deaths by COVID-19, J. Environ. Econ. Manag. 108 (2021), 102448, https://doi.org/10.1016/j.jeem.2021.102448.

[17] A.V. Raveendran, R. Jayadevan, S. Sashidharan, Long COVID: an overview, Diabetes Metab. Syndr.: Clin. Res. Rev. 15 (2021) 869–875, https://doi.org/10.1016/j.dsx.2021.04.007.

[18] H. Crook, S. Raza, J. Nowell, M. Young, P. Edison, Long COVID—mechanisms, risk factors, and management, BMJ (2021) 374, https://doi.org/10.1136/bmj.n1648.

[19] C. Chatterjee, A. Sen, Sensitive colorimetric sensors for visual detection of carbon dioxide and sulfur dioxide, J. Mater. Chem. A 3 (2015) 5642, https://doi.org/10.1039/C4TA06321J.

[20] T.-V. Dinh, I.-Y. Choi, Y.-S. Son, J.-C. Kim, A review on non-dispersive infrared gas sensors: improvement of sensor detection limit and interference correction, Sens. Actuators B 231 (2016) 529–538, https://doi.org/10.1016/j.snb.2016.03.040.

[21] X. Jia, J. Roels, R. Baets, G. Roelkens, On-chip non-dispersive infrared CO_2 sensor on an integrating cylinder, Sensors 19 (2019) 4260, https://doi.org/10.3390/s19194260.

[22] G. Alberti, C. Zanoni, L.R. Magnaghi, R. Biesuz, Disposable and low-cost colorimetric sensors for environmental analysis, Int. J. Environ. Res. Public Health 17 (2020) 8331, https://doi.org/10.3390/ijerph17228331.

[23] B. Liu, J. Zhuang, G. Wei, Recent advances in the design of colorimetric sensors for environmental monitoring, Environ. Sci. Nano 7 (2020) 2195, https://doi.org/10.1039/D0EN00449A.

[24] A.K. Davey, X. Gao, Y. Xia, Z. Li, M.N. Dods, S. Delacruz, A. Pan, S. Swamy, D. W. Gardner, C. Carraro, R. Maboudian, Amine-functionalized metal-organic framework ZIF-8 toward colorimetric CO_2 sensing in indoor air environment, Sens. Actuators B: Chem. (2021), 130313, https://doi.org/10.1016/j.snb.2021.130313.

[25] H.-C. Zhou, J.R. Long, O.M. Yaghi, Introduction to metal-organic frameworks, Chem. Rev. 112 (2) (2012) 673–674, https://doi.org/10.1021/cr300014x.

[26] M. Bergaoui, M. Khalfaoui, A. Awadallah-F, Al-Muhtaseb, A review of the features and applications of ZIF-8 and its derivatives for separating CO_2 and isomers of C_3- and C_4. hydrocarbons, J. Nat. Gas. Sci. Eng. 96 (2021), 104289, https://doi.org/10.1016/j.jngse.2021.104289.

[27] X. Gong, Y. Wang, T. Kuang, ZIF-8-based membranes for carbon dioxide capture and separation, ACS Sustain. Chem. Eng. 5 (2017) 11204–11214, https://doi.org/10.1021/acssuschemeng.7b03613.

[28] J. Perez-Pellitero, H. Amrouche, F.R. Siperstein, G. Pirngruber, C. Nieto-Draghi, G. Chaplais, A. Simon-Masseron, D. Bazer-Bachi, D. Peralta, N. Bats, Adsorption of CO_2, CH_4, and N_2 on zeolitic imidazolate frameworks: experiments and simulations, Chem. Eur. J. 16 (2010) 1560–1571, https://doi.org/10.1002/chem.200902144.

[29] Y. Sahin, H. Kacus, S. Aydogan, M. Yilmaz, U. Incekara, Enhanced electrical and optical characteristics of Co/Phenol red (PR)/Silicon hybrid heterojunction for photodiode and thermal applications, J. Electron. Mater. 49 (2020) 8, https://doi.org/10.1007/s11664-020-08217-4.

[30] Web reference two. Held, P. Using Phenol Red to Assess pH in Tissue Culture Media. Using the Cytation 5 Cell Imaging Microplate Reader to Monitor Cell Culture. Biotek¸ 2018. ⟨https://www.biotek.com/resources/application-notes/using-phenol-red-to-assess-ph-in-tissue-culture-media/⟩ (accessed 2021/2/1).

[31] R. Ben Said, J.M. Koelle, K. Essalah, B. Tangour, A. Sayari, Unified approach to CO_2-amine reaction mechanisms, ACS Omega 5 (2020) 26125–26133, https://doi.org/10.1021/acsomega.0c03727.

[32] H.G. Hecht, The interpretation of diffuse reflectance spectra, J. Res. Natl. Bur. Stand. A Phys. Chem. 80 (4) (1976) 567–583. DOI: https://dx.doi.org/10.6028%2Fjres.080A.056.

[33] Web reference three. Acetone: The National Institute for Occupational Safety and Health (NIOSH). CDC. U.S. Department of Health & Human Services. ⟨https://www.cdc.gov/niosh/npg/npgd0004.html⟩ (accessed 2022/18/3).

[34] Web reference four. Ethyl alcohol: The National Institute for Occupational Safety and Health (NIOSH). CDC. U.S. Department of Health & Human Services. ⟨https://www.cdc.gov/niosh/npg/npgd0262.html⟩ (accessed 2022/18/3).

[35] Web reference five. CSD Single Crystal CCDC VELVOY. CCDC. 602542. ⟨https://www.ccdc.cam.ac.uk/structures/search?identifier=VELVOY⟩ (accessed 2022/18/1).

[36] Y. Zhang, Y. Jia, L. Hou, Synthesis of zeolitic imidazolate framework-8 on polyester fiber for $PM_{2.5}$ removal, Rsc. Adv. 8 (2018) 31471–31477, https://doi.org/10.1039/C8RA06414H.

[37] C. Zhang, C. Han, D.S. Sholl, J.R. Schmidt, Computational characterization of defects in metal-organic frameworks: spontaneous and water-induced point defects in ZIF-8, J. Phys. Chem. Lett. 7 (3) (2016) 459–464, https://doi.org/10.1021/acs.jpclett.5b02683.

[38] X. Liu, M. Kozlowska, T. Okkali, D. Wagner, T. Higashino, Brenner-Weiß, S. M. Marschner, Z. Fu, Q. Zhang, H. Imahori, S. Brase, W. Wenzel, C. Wçll, L. Heinke, Photoconductivity in metal-organic framework (MOF) thin films, Angew. Chem. Int. Ed. 58 (2019) 9590–9595, https://doi.org/10.1002/anie.201904475.

[39] F.-Y. Yi, Y. Wang, J.-P. Li, D. Wu, Y.-Q. Lan, Z.-M. Sun, An ultrastable porous metal-organic framework switch towards aromatic compounds, Mater. Horiz. 2 (2015) 245, https://doi.org/10.1039/C4MH00210E.

[40] D.N. Ta, H.K.D. Nguyen, B.X. Trinh, Q.T.N. Le, H.N. Ta, H.T. Nguyen, Preparation of Nano-ZIF-8 in methanol with high yield, Can. J. Chem. Eng. 96 (2018) 1518–1530, https://doi.org/10.1002/cjce.23155.

[41] M. Zhong, L. Kong, K. Zhao, Y.-H. Zhang, N. Li, X.-H. Bu, Recent progress of nanoscale metal-organic frameworks in synthesis and battery applications, Adv. Sci. 8 (2021), 2001980, https://doi.org/10.1002/advs.202001980.

[42] M.J. Van Vleet, T. Weng, X. Li, J.R. Schmidt, In situ, time-resolved, and mechanistic studies of metal-organic framework nucleation and growth, Chem. Rev. 118 (2018) 3681–3721, https://doi.org/10.1021/acs.chemrev.7b00582.

[43] M.N. Shahrak, M. Gharamaninezhad, M. Eydifarash, Zeolitic imidazolate framework-8 for efficient adsorption and removal of Cr(VI) ions from aqueous solution, Environ. Sci. Pollut. Res. 24 (2017) 9624–9634, https://doi.org/10.1007/s11356-017-8577-5.

[44] H. Kaur, G.C. Mohanta, V. Gupta, D. Kukkar, S. Tyagi, Synthesis and characterization of ZIF-8 nanoparticles for controlled release of 6-mercaptopurine drug, J. Drug Deliv. Sci. Technol. 41 (2017) 106–112, https://doi.org/10.1016/j.jddst.2017.07.004.

[45] Web reference six. Spectroscopy Tutorial: Reference. Table of Characteristic IR Absorptions. ⟨http://www.orgchemboulder.com/Spectroscopy/specttutor/irchart.shtml⟩. (accessed 21/1/2022).

[46] Web reference seven. 24.10: Spectroscopy of Amines. Chemistry LibreTextstM, 2021. https://chem.libretexts.org/Bookshelves/Organic_Chemistry/Organic_Chemistry_(McMurry)/24%3A_Amines_and_Heterocycles/24.10%3A_Spectroscopy_of_Amines. (accessed 21/1/2022).

[47] H. Bunzen, Chemical stability of metal-organic frameworks for applications in drug delivery, ChemNanoMat (2021) 998–1007, https://doi.org/10.1002/cnma.202100226.

[48] H. Zhang, M. Zhao, Y.S. Lin, Stability of ZIF-8 in water under ambient conditions, Microporous Mesoporous Mater. 279 (2019) 201–210, https://doi.org/10.1016/j.micromeso.2018.12.035.

[49] S. Tanaka, Y. Tanaka, A simple step toward enhancing hydrothermal stability of ZIF-8, ACS Omega 4 (2019) 19905–19912, https://doi.org/10.1021/acsomega.9b02812.

[50] K. Cui, S. Bhattacharyya, S. Nair, J.R. Schmidt, Origins of acid-gas stability behavior in zeolitic imidazolate frameworks: the unique high stability of ZIF-71, J. Am. Chem. Soc. 143 (2021) 18061–18072, https://doi.org/10.1021/jacs.1c06321.

[51] G.F. Versteeg, L.A.J. Van Dijck, W.P.M. Van Swaaij, On the kinetics between CO_2 and alkanolamines both in aqueous and nonaqueous solutions. an overview, Chem. Eng. Comm. Vol. 144 (1996) 113–158, https://doi.org/10.1080/00986449608936450.

[52] B. Lv, B. Guo, Z. Zhou, G. Jing, Mechanisms of CO_2 capture into monoethanolamine solution with different CO_2 loading during the absorption/desorption processes, Environ. Sci. Technol. 49 (2015) 10728–10735, https://doi.org/10.1021/acs.est.5b02356.

[53] S.A. Didas, A.R. Kulkarni, D.S. Sholl, C.W. Jones, Role of amine structure on carbon dioxide adsorption from ultradilute gas streams such as ambient air, ChemSusChem 5 (2012) 2058–2064, https://doi.org/10.1002/cssc.201200196.

[54] M. Wickenhisser, F. Jeremias, S.K. Henninger, C. Janiak, Grafting of hydrophilic ethylene glycols or ethylenediamine on coordinatively unsaturated metal sites in MIL-100(Cr) for improved water adsorption characteristics, Inorg. Chim. Acta 407 (2013) 145–152, https://doi.org/10.1016/j.ica.2013.07.024.

[55] Z.A. Siefker, J.N. Hodul, X. Zhao, N. Bajaj, K.M. Brayton, C. Flores-Hansen, W. Zhao, G.T.-C. Chiu, J.E. Braun, J.F. Rhoads, B.W. Boudouris, Manipulating polymer composition to create low-cost, high-fidelity sensors for indoor CO_2

monitoring, Sci. Rep. 11 (2021) 13237, https://doi.org/10.1038/s41598-021-92181-4.

[56] Y. Sun, Y. Li, J.-C. Tan, Framework flexibility of ZIF-8 under liquid intrusion: discovering time-dependent response and structural relaxation, Phys. Chem. Chem. Phys. 20 (2018) 10108, https://doi.org/10.1039/C8CP00447A.

[57] D. Fairen-Jimenez, S.A. Moggach, M.T. Wharmby, P.A. Wright, S. Parsons, T. Duren, Opening the gate: framework flexibility in ZIF-8 explored by experiments and simulations, J. Am. Chem. Soc. 133 (23) (2011) 8900–8902, https://doi.org/10.1021/ja202154j.

[58] K. Zhang, R.P. Lively, C. Zhang, R.R. Chance, W.J. Koros, D.S. Shol, S. Nair, Exploring the framework hydrophobicity and flexibility of ZIF-8: from biofuel recovery to hydrocarbon separations, J. Phys. Chem. Lett. 4 (21) (2013) 3618–3622, https://doi.org/10.1021/jz402019d.

[59] Y. Hu, Z. Liu, J. Xu, Y. Huang, Y. Song, Evidence of pressure enhanced CO_2 storage in ZIF-8 probed by FTIR spectroscopy, J. Am. Chem. Soc. 135 (2013) 9287–9290, https://doi.org/10.1021/ja403635b.

[60] A. Schejn, L. Balan, V. Falk, L. Aranda, G. Medjahdi, R. Schneider, Controlling ZIF-8 nano- and microcrystal formation and reactivity through zinc salt variations, CrystEngComm 16 (2014) 4493, https://doi.org/10.1039/C3CE42485E.

[61] D.K. Panchariya, R.K. Rai, E.A. Kumar, S.K. Singh, Core-shell zeolitic imidazolate frameworks for enhanced hydrogen storage, ACS Omega 3 (2018) 167–175, https://doi.org/10.1021/acsomega.7b01693.

[62] J. Dai, X. Xiao, S. Duan, J. Liu, J. He, J. Lei, L. Wang, Synthesis of novel microporous nanocomposites of ZIF-8 on multiwalled carbon nanotubes for adsorptive removing benzoic acid from water, Chem. Eng. J. 331 (2018) 64–74, https://doi.org/10.1016/j.cej.2017.08.090.

[63] X. Mei, S. Yang, P. Lu, Y. Zhang, J. Zhang, Improving the selectivity of ZIF-8/Polysulfone-mixed matrix membranes by polydopamine modification for H_2/CO_2 separation, Front. Chem. (2020), https://doi.org/10.3389/fchem.2020.00528.

[64] M.S. Khan, M. Khalid, M. Shahid, What triggers dye adsorption by metal organic frameworks? The current perspectives, Mater. Adv. 1 (2020) 1575, https://doi.org/10.1039/D0MA00291G.

[65] V. Ka-Man-Au, Recent advances in the use of metal-organic frameworks for dye adsorption, Front. Chem. 8 (2020) 708, https://doi.org/10.3389/fchem.2020.00708.

[66] C. Nanthamathee, P. Dechatiwongse, Kinetic and thermodynamic studies of neutral dye removal from water using zirconium metal-organic framework analogues, Mater. Chem. Phys. 258 (2021), 123924, https://doi.org/10.1016/j.matchemphys.2020.123924.

[67] Y. Feng, Y. Li, M. Xu, S. Liu, J. Yao, Fast adsorption of methyl blue on zeolitic imidazolate framework-8 and its adsorption mechanism, RSC Adv. 6 (2016), 109608, https://doi.org/10.1039/C6RA23870J.

[68] S.V. Van Cleuvenbergen, Z.J. Smith, O. Deschaume, C. Bartic, S. Waschmann-Hogiu, T. Verbiest, M.A. van der Veen, Morphology and structure of ZIF-8 during crystallization measured by dynamic angle-resolved second harmonic scattering, Nat. Commun. 9 (2018) 3418, https://doi.org/10.1038/s41467-018-05713-.

[69] W.T.S. Cole, H. Wei, S.C. Nguyen, C.B. Harris, D.J. Miller, R.J. Saykally, Dynamics of micropollutant adsorption to polystyrene surfaces probed by angle-resolved second harmonic scattering, J. Phys. Chem. C. 123 (23) (2019) 14362–14369, https://doi.org/10.1021/acs.jpcc.9b01146.

[70] R.K. Campen, D.-s Zheng, H.-f Wang, E. Borguet, Second harmonic generation as a probe of multisite adsorption at solid-liquid interfaces of aqueous colloid suspensions, J. Phys. Chem. C. 111 (25) (2007) 8805–8813, https://doi.org/10.1021/jp061730h.

[71] A.G.F. de Beer, S. Roke, Obtaining molecular orientation from second harmonic and sum frequency scattering experiments in water: angular distribution and polarization dependence, J. Chem. Phys. 132 (2010), 234702, https://doi.org/10.1063/1.3429969.

[72] T. Lewis, M. Faubel, B. Winter, J.C. Hemminger, CO_2 capture in amine-based aqueous solution: role of the gas-solution interface, Angew. Chem. Int. Ed. 50 (2011) 10178–10181, https://doi.org/10.1002/anie.201101250.

[73] J.J. Gassensmith, H. Furukawa, R.A. Smaldone, R.S. Forgan, Y.Y. Botros, O. M. Yaghi, J.F. Stoddart, Strong and reversible binding of carbon dioxide in a green metal-organic framework, J. Am. Chem. Soc. 133 (2011) 15312–15315, https://doi.org/10.1021/ja206525x.

[74] K.I. Hadjivanov, D.A. Panayotov, M.Y. Mihaylov, E.Z. Ivanova, K.K. Chakarova, S. M. Andonova, N.L. Drenchev, Power of infrared and raman spectroscopies to characterize metal-organic frameworks and investigate their interactions with guest molecules, Chem. Rev. 121 (2021) 1286–1424, https://doi.org/10.1021/acs.chemrev.0c00487.

Adrian K. Davey is currently a Ph.D. Candidate in Chemical & Biomolecular Engineering at the University of California, Berkeley. Adrian's research interests center metal-organic framework-based colorimetric gas sensing toward an improved monitoring of indoor air pollutants.

Zhou Li is a postdoctoral researcher in the Department of Aeronautics and Astronautics at Stanford University. He received his B.S. from Central South University in 2014 and PhD degree from University of Science and Technology of China in Safety Science and Technology in 2021. During 2019–2021, he worked as a visiting graduate researcher with Prof. Roya Maboudian in the Department of Chemical and Biomolecular Engineering at University of California, Berkeley. His current research interest is mainly on semiconductor gas sensors.

Natalie Lefton is currently pursuing a Ph.D. in Chemical & Biomolecular Engineering at the University of California, Berkeley. Her research focuses on the characterization and kinetic studies of metal-exchanged zeolite catalysts to develop structure-function relationships.

Branden E. Leonhardt is currently a Ph.D. Candidate in Chemical & Biomolecular Engineering at the University of California, Berkeley. Branden's research interests include studying silica-supported catalysts and understanding the fundamental interactions between adsorbates and solid surfaces using computational chemistry.

Alireza Pourghaderi is pursuing his Ph.D. in Chemical and Biomolecular Engineering at the University of California, Berkeley. Currently, his research focuses on metal-organic frameworks (MOFs) and their electrical and chemical sensing applications.

Stuart McElhany is currently pursuing a Ph.D. in Chemical and Biomolecular Engineering at the University of California, Berkeley. His research interests involve the sequestration of carbon in cement-based composites towards creating sustainable construction materials.

Derek Popple is currently pursuing a PhD in Chemistry at the University of California Berkeley. His research focuses on the synthesis of low-dimensional nanomaterials and transmission electron microscopy.

Chunhui Dai is a Postdoctoral Scholar working with Prof. Alex Zettl in the Materials Sciences Division at Lawrence Berkeley National Laboratory and Department of Physics at the University of California, Berkeley. He received his Ph.D. from University of Minnesota Twin Cities. His research is focused on kirigami/origami engineering of the nanoscale sensors and actuators.

Salman Kahn is a Research Affiliate at the University of California, Berkeley and Lawrence Berkeley National Laboratory. His research interest involves understanding the interplay between topology and correlations in Van der Waals heterostructures.

Matthew N. Dods is currently pursuing a Ph.D. in Chemical & Biomolecular Engineering at the University of California, Berkeley. His research is concerned with the synthesis and characterization of metal-organic frameworks for a variety of applications.

Alex Zettl is a is a Professor of Physics at the University of California, Berkeley and a Senior Scientist at the Lawrence Berkeley National Laboratory. He received his Ph.D. in experimental condensed matter physics from the University of California, Los Angeles. His research is focused on investigating electronic, magnetic and mechanical properties of nanoscale materials.

Carlo Carraro is an Adjunct Professor of Chemical & Biomolecular Engineering at the University of California, Berkeley. His research interests are in surface science, nanometrology, and microsystems technology.

Roya Maboudian is a Professor of Chemical & Biomolecular Engineering at the University of California, Berkeley and Co-Director of the Berkeley Sensor and Actuator Center (BSAC). Her research interest is in the surface/interface and materials science and engineering of micro/nanosystems, with applications in harsh-environment sensing, health and environmental monitoring, and energy technologies.